Automotive Innovation (2023) 6:414–424
https://doi.org/10.1007/s42154-023-00226-3

# Thermal Runaway Characteristics and Modeling of $LiFePO_4$ Power Battery for Electric Vehicles

**Tao Sun[1] · Luyan Wang[1] · Dongsheng Ren[2,3] · Zhihe Shi[1] · Jie Chen[3] · Yuejiu Zheng[1,3] · Xuning Feng[3] · Xuebing Han[3] · Languang Lu[3] · Li Wang[2,3] · Xiangming He[2,3] · Minggao Ouyang[3]**

Received: 30 June 2022 / Accepted: 20 March 2023 / Published online: 4 August 2023


## Abstract

$LiFePO_4$ (LFP) lithium-ion batteries have gained widespread use in electric vehicles due to their safety and longevity, but thermal runaway (TR) incidents still have been reported. This paper explores the TR characteristics and modeling of LFP batteries at different states of charge (SOC). Adiabatic tests reveal that TR severity increases with SOC, and five stages are identified based on battery temperature evolution. Reaction kinetics parameters of exothermic reactions in each TR stage are extracted, and TR models for LFP batteries are established. The models accurately simulate TR behaviors at different SOCs, and the simulated TR characteristic temperatures also agree well with the experimental results, with errors of TR characteristic temperatures less than 3%. The prediction errors of TR characteristic temperatures under oven test conditions are also less than 1%. The results provide a comprehensive understanding of TR in LFP batteries, which is useful for battery safety design and optimization.

**Keywords** Lithium-ion battery · Safety · Thermal runaway · Thermal runaway model · State of charge

## Abbreviations

| | |
|---|---|
| ARC | Accelerating rate calorimeter |
| EV-ARC | Extended-volume accelerating rate calorimetry |
| LFP | $LiFePO_4$ |
| NMC | $LiNi_xMn_yCo_zO_2$ |
| SEI | Solid electrolyte interface |
| SOC | State of charge |
| TR | Thermal runaway |

## 1 Introduction

Lithium-ion battery is the most commonly used energy storage device for electric vehicles due to its high energy density, low self-discharge, and long lifespan [1–3]. The performance of lithium-ion power battery systems largely determines the development level of pure electric vehicles [4–6]. Despite of its popularity, safety incidents caused by thermal runaway (TR) have limited its widespread use [7–9]. As a safer alternative, lithium iron phosphate (LFP) cathode batteries offer high energy and power density and long cycle life [10, 11], making them widely used in transportation and stationary energy storage [1]. LFP batteries have relatively lower energy density but better safety performance compared to $LiNi_xMn_yCo_zO_2$ (NMC) batteries. In May 2021, the output of LFP batteries for electric vehicles in China has surpassed that of NMC batteries [12]. However, fire accidents of electric vehicles caused by TR of LFP batteries have also been reported [13]. The TR in LFP batteries is still of concern.

TR in LFP batteries can be caused by several factors, including electrical abuse (overcharge, over-discharge, external short circuit), mechanical abuse (nail penetration, crush), and thermal abuse (overheat) [14–16]. Sun et al. [17] explored the effects of overcharging on TR for a LFP battery and found that stopping the overcharge after the safety valve opens can effectively suppress battery TR. Similarly,

Academic Editor: Lei Zhang

✉ Dongsheng Ren
rends@tsinghua.edu.cn

✉ Yuejiu Zheng
yuejiu_zheng@163.com

[1] School of Mechanical Engineering, University of Shanghai for Science and Technology, Shanghai 200093, China

[2] Institute of Nuclear and New Energy Technology, Tsinghua University, Beijing 100084, China

[3] State Key Laboratory of Automotive Safety and Energy, Tsinghua University, Beijing 100084, China

Fernandes et al. [18] studied the overcharge-induced TR in LFP batteries and quantitatively identified the gases generated during the TR process. Huang et al. [19] investigated the influences of the state of charge (SOC), penetration position, penetration depth, penetration speed, and nail diameter on the TR behaviors for LFP batteries during nail penetration, and found that the trigger of TR was more related to the penetration location. Zaghib et al. [20] studied the safety performance of lithium-ion batteries with carbon-coated LFP cathode using differential scanning calorimeter (DSC) and accelerating rate calorimetry (ARC), and found that the LFP cathode was safer than the commonly used lithium metal oxide cathodes with layered and spinel structures. Liu et al. [21] investigated the TR process and the fire behaviors for a 22 Ah LFP/graphite battery and revealed the relationship between TR and fire behaviors under different SOCs. Bugryniec et al. [22] compared the TR behaviors for LFP and NMC batteries under oven tests and concluded that LFP batteries were more stable than NMC batteries.

In addition to experimental studies, several models have been developed to investigate the TR behaviors in lithium-ion batteries. For instance, Hatchard et al. [23] established a TR model for $LiCoO_2$ batteries to predict the battery performance during oven tests, which was later expanded into a 3-dimensional (3D) thermal abuse model by Kim et al. [24] to capture battery temperature distribution during the TR process. Moreover, Feng et al. [25] and Ren et al. [26] developed TR models for NMC batteries. Multi-scale models were also built to simulate the TR behaviors of lithium-ion batteries under various abuse conditions [27–29]. However, most TR models of lithium-ion batteries focused on NMC batteries. There are only a limited number of studies conducted for LFP batteries. For example, Guo et al. [30] investigated the temperature distribution inside a LFP battery under abuse conditions using a 3D thermal finite element model. Analogously, Peng et al. [31] studied the thermal safety of LFP batteries by modeling approach. Mei et al. [32] established oven TR models at six different temperatures to analyze TR characteristics and temperature distribution in large-scale LFP batteries under high-temperature heating conditions. Despite of above efforts, the existing TR models for LFP batteries are established using reaction kinetics parameters derived from the thermal reactions in NMC batteries. That greatly reduces the accuracy and credibility of those TR models in simulating the TR behaviors of LFP batteries, as LFP and NMC batteries behave totally different under various safety tests. Therefore, an accurate TR model for LFP battery based on its reaction mechanism is urgently needed for safety design and optimization of LFP battery.

The remainder of this paper is structured as follows. Section 2 introduces the battery model and experimental equipment. Section 3 presents the adiabatic TR tests for exploring the TR behaviors of LFP batteries at the SOC levels of 25%, 50%, 75%, and 100%. Section 4 provides details on a developed TR model for LFP batteries at different SOCs and its validation based on comprehensive simulation and experimental data. Finally, Sect. 5 concludes this study and offers a brief discussion on future research direction.

**Table 1** Basic information about the LFP battery

| Parameter | Value |
|---|---|
| Cathode material | $LiFePO_4$ |
| Anode material | Graphite |
| Operating voltage | 2.5–3.65 V |
| Capacity | 50 A·h |
| Energy density | 160 Wh/kg |
| Size | 160 × 140 × 13 mm |
| Weight | 1120 g |

## 2 TR Experiments at Different SOCs

### 2.1 Battery Information

The study utilizes a commercial prismatic LFP power battery, it has a capacity of 50 A·h and dimensions of 160×140×13 mm, as listed in Table 1. The battery's energy density is around 160 Wh/kg.

### 2.2 TR Tests Using Accelerating Rate Calorimetry

The TR behavior in LFP battery is explored using the extended-volume accelerating rate calorimetry (EV-ARC) to simulate an adiabatic environment. The ARC test revealed the TR characteristics of the battery, including the characteristic temperatures and kinetic parameters of the exothermic reactions. The EV-ARC system used in this paper is manufactured by Thermal Hazard Technology (THT) and has a diameter of 25 cm and a depth of 50 cm, as shown in Fig. 1(a). The battery is placed in the central zone of the EV-ARC system, as presented in Fig. 1(b). The temperature change of the battery is monitored by a N-type thermocouple (main thermocouple) of EV-ARC attached to the center surface of the battery. To detect the internal temperature during TR, a K-type thermocouple is inserted into the battery using the method presented in Ref. [33].

The EV-ARC system operates in "heat-wait-search" mode [34] until the battery's self-heating rate exceeds 0.02 °C·min$^{-1}$, then enters the adiabatic mode to monitor and maintain adiabatic conditions until TR occurs. Table 2 lists the experiment settings of the EV-ARC tests. EV-ARC tests are performed on 4 batteries at different SOCs (25%, 50%, 75%. and 100% SOC).

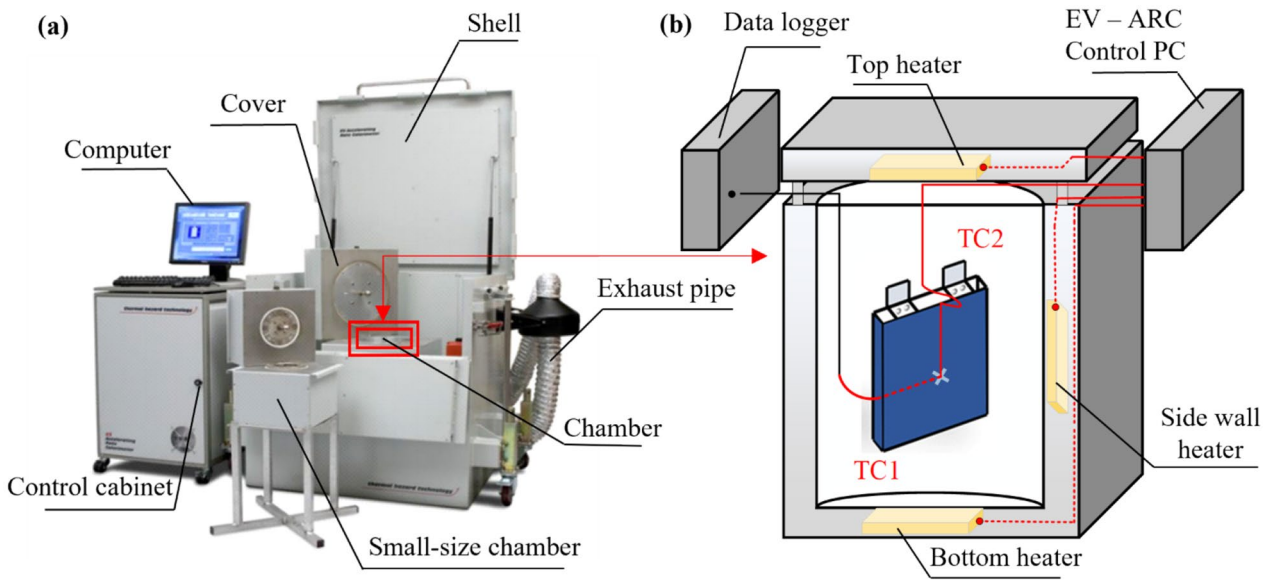


**Fig. 1** EV-ARC System and test setup: **a** Equipment, **b** Test configuration

## 3 Analysis and Discussion of TR Experiment Results

### 3.1 Analysis of Battery TR Characteristics

Fig. 2 shows the ARC test results of the LFP battery at 25%, 50%, 75%, and 100% SOC. Fig. 2(a) depicts a stepwise temperature rise at the beginning of the test for the battery at 25% SOC due to the EV-ARC system's "heat-wait-seek" mode. The EV-ARC system enters the adiabatic mode at 106.2 °C, but returns to the "heat-wait-seek" cycle at around 110.8 °C as the battery's self-heating rate drops below 0.02 °C·min$^{-1}$. The alternation between adiabatic mode and the "heat-wait-seek" cycle is repeated several times due to weak exothermic reactions inside the battery and limited heat dissipation of the EV-ARC system. Onset temperature of self-heating ($T_1$) of the 25% SOC battery is determined as 151.1 °C after EV-ARC re-enters and stays in adiabatic mode. The battery voltage remains stable before the battery temperature reached $T_1$, except for a minor fluctuation at 141 °C. It drops sharply to 0.271 V at 230 °C due to internal short circuit, causing significant heat generation and temperature rise. However, the maximum temperature rate of the 25% SOC battery remains below 5 °C·min$^{-1}$, indicating no severe TR inside the battery. The EV-ARC system continues heating the battery in "heat-wait-search" cycle until reaching 300 °C, and the experiment stops.

The battery at 50% SOC exhibits similar TR behavior as the battery at 25% SOC, as shown in Fig. 2(b). It exhibits a $T_1$ of 136.1 °C, and experiences a massive internal short circuit at 234.6 °C, leading to a sharp rise in temperature rate to 6.76 °C·min$^{-1}$. The maximum temperature of the 50% SOC battery reaches 305.8 °C, higher than that of the 25% SOC, due to its larger amount of energy stored inside the battery. Figure 2(c) shows that the 75% SOC battery exhibits a $T_1$ of 135.9 °C, close to that of the 50% SOC battery. The battery voltage fluctuates significantly as the temperature rises above 140 °C, indicating ongoing internal short circuit. The battery voltage drops abruptly to 0 V at 228.6 °C, leading to a rapid increase in temperature to 496.2 °C. The ARC test result of the battery at 100% SOC is presented in Fig. 2(d). The 100% SOC battery exhibits a $T_1$ of 135.9 °C and fluctuating voltage after $T_1$. The battery voltage drops to 0 V at 220.7 °C, causing a significant increase in temperature to 619.9 °C.

**Table 2** Key parameters of EV-ARC tests

| Parameter | Value |
|---|---|
| Start temperature | 40 ℃ |
| End temperature | 300 ℃ |
| Temperature step | 5 ℃ |
| Temp rate sensitivity | 0.02 °C·min$^{-1}$ |
| Wait time | 60 min |
| Seek time | 20 min |

Figure 3 compares the temperature rise rate profiles of batteries under different SOC levels during ARC tests. In the early stage of the tests, the temperature rise rates of the batteries at different SOCs overlap, indicating similar exothermic reactions (likely the decomposition of solid electrolyte interface (SEI) and reactions between lithiated graphite and electrolyte [35–37]) in the early stage of TR. With the increase of SOC, the battery temperature rise rate gradually

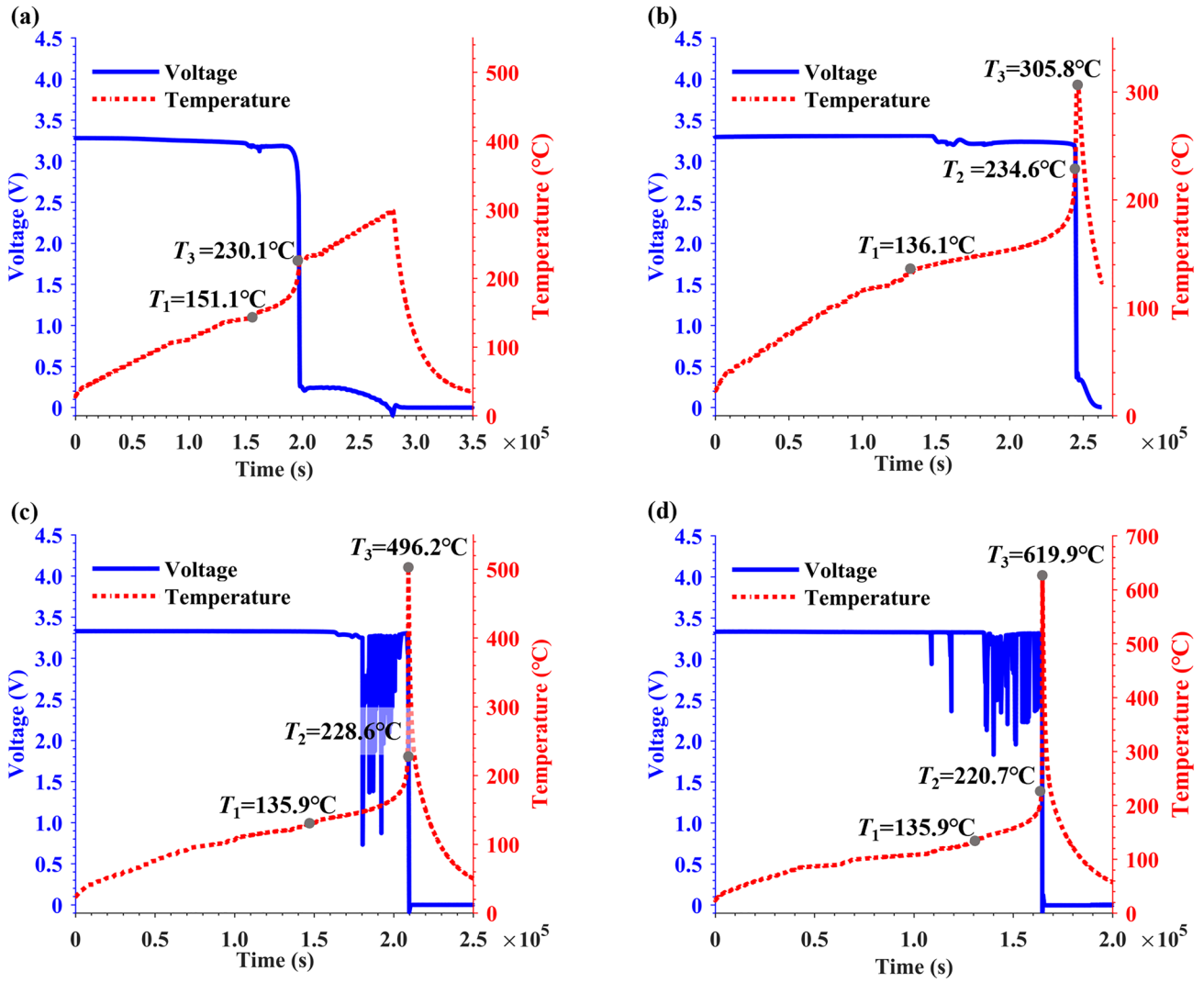


**Fig. 2** ARC test results of LFP batteries at different SOCs: **a** 25% SOC, **b** 50% SOC, **c** 75% SOC and **d** 100% SOC

increases, with the maximum temperature rate varying. For a battery at 25% SOC, the maximum temperature rise rate is 1.779 °C·min$^{-1}$, below the TR criterion of 5 °C·min$^{-1}$, indicating no serious TR at 25% SOC. As SOC increases, the maximum temperature rise rate increases sharply, with those of the batteries at 50%, 75%, and 100% SOC reaching 6.76, 237.3, and 953.2 °C·min$^{-1}$, respectively, demonstrating severe TR inside the batteries.

Three characteristic temperatures (onset temperature of self-heating $T_1$, trigger temperature of TR $T_2$, and maximum temperature of TR $T_3$) can be derived from ARC test results to evaluate battery TR performance. $T_1$ is the temperature at which the battery's self-heating rate is higher than 0.02 °C·min$^{-1}$. In this study, $T_1$ is determined by the temperature after which the ARC system stays in the adiabatic mode to eliminate measurement error. $T_1$ is significant for the battery's thermal management strategy as the thermal management system should keep the temperature below $T_1$ during normal operation to avoid severe side reactions. $T_2$ is defined as the temperature at which the battery's self-heating rate is higher than 5 °C·min$^{-1}$, considering the lower severity of the TR in LFP batteries compared to NCM batteries. $T_3$ is the maximum temperature during the TR process and reflects the amount of energy released during the process.

Figure 4 compares the TR characteristic temperatures of batteries at different SOCs. The battery's $T_1$ declines from 151.1 ℃ to 136.1 ℃ as the SOC increases from 25% to 50%, and remains constant at around 136 ℃. The onset of self-heating is usually caused by the decomposition of SEI film [38]. The decline of $T_1$ with the increased SOC indicates that the SEI film on the anode surface becomes more unstable at a higher SOC. The battery's $T_2$ also decreases slightly as SOC increases from 50% to 100% SOC. However, the

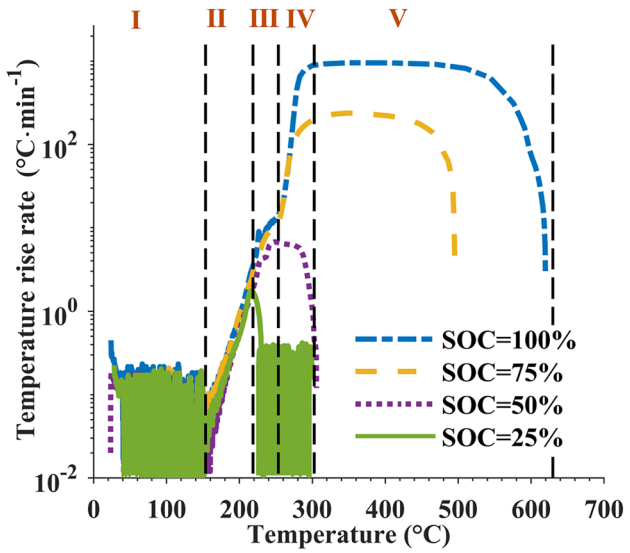


**Fig. 3** Temperature rise rate profiles of batteries at different SOCs

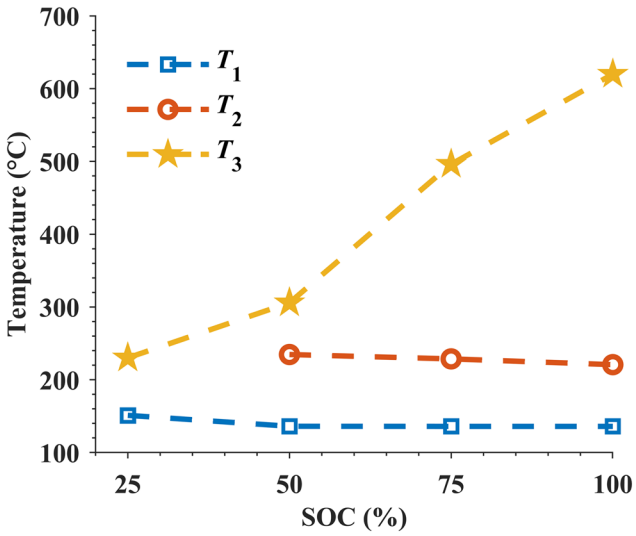


**Fig. 4** TR characteristic temperatures of batteries at different SOCs

25% SOC battery doesn't undergo TR with a maximum temperature rate of 1.779 °C·min$^{-1}$. The maximum temperature $T_3$ significantly increases as the battery's SOC rises from 25% to 100%, indicating an increase in the total energy released during TR. Moreover, as presented in Fig. 3, the maximum temperature rise rate also increases dramatically with the increasing SOC. The maximum temperature rate of the 100% SOC battery is about 535 times greater than that of the 25% SOC battery. This rapid increase of $T_3$ and the maximum temperature rate demonstrate that the LFP battery poses a much higher TR hazard at high SOC, mainly due to the increased amount of stored electrochemical energy. Therefore, reducing the battery's SOC can be an effective solution for reducing the TR hazard in LFP battery.

### 3.2 Five-Stages TR Process of LFP Battery

The TR process in the LFP battery can be divided into 5 stages, as shown in Fig. 3, according to the experimental results.

Stage I ($T < T_1$): Before the battery temperature reaches $T_1$, the temperature rise of the battery primarily originated from the heat exchange with the EV-ARC system, with the apparent stepwise temperature changes induced by the "heat-wait-search" mode, as shown in Fig. 2. Few side reactions happen inside the battery in this stage, and the battery voltage stays almost constant.

Stage II ($T_1 < T < T_2$): When the battery temperature reaches $T_1$, the ARC system detects self-heating in the battery and tracks its temperature change. Generally, the onset of self-heating in lithium-ion battery is induced by the decomposition of the SEI film on the anode [39]. Once the SEI film cannot protect the direct exposure of the anode to the electrolyte, the lithiated anode will further react with the electrolyte [40, 41], leading to a continuous rise in battery temperature rate. As shown in Fig. 3, the temperature rate profiles of batteries at different SOCs overlap, indicating similar exothermic reactions. The battery voltage decreases slightly in Stage II, mainly due to the side reactions in the anode. As the temperature goes higher, the battery voltage begins to fluctuate because of separator shrinkage and slight internal short circuit. The TR process of the 25% SOC stops in Stage II, due to limited stored electrochemical energy.

Stage III ($T_2 < T < 261$ ℃): As the battery temperature rate surpasses 5 °C·min$^{-1}$, severe TR is identified. The safety valve of the prismatic battery opens in this stage, leading to the venting of the gases generated from the exothermic reactions and some of the electrolyte. The venting behavior will also change the reaction rate of exothermic reactions inside the battery, resulting in a slight decrease in the slope of the temperature rise rate profiles. The battery voltage continues to fluctuate in this stage.

Stage IV (261 ℃ $< T <$ 302 ℃): As the venting process finishes, the battery temperature rise rate increases rapidly again, bringing the temperature rise rate to above 100 °C·min$^{-1}$, as seen in the temperature rate profiles of batteries at 75% and 100% SOC. The battery with 50% SOC, which has lower energy, moves directly to Stage V and skips Stage IV.

Stage V (302 ℃ $< T < T_3$): Massive internal short circuit occurs in Stage V, and the battery voltage drops to 0 V. This leads to significant heat generation during massive internal short circuit, leading to a high and sustained temperature rate, resulting in a sharp increase in battery temperature to its maximum value.

## 4 TR Model Development and Validation

### 4.1 TR Model

#### 4.1.1 Reaction Kinetics Model

In this section, the reaction kinetics model is established based on adiabatic TR test results in Sect. 3. Firstly, during the adiabatic test, the temperature rise rate of the battery $\frac{dT}{dt}$ originated from the exothermic side reaction is directly proportional to the change of the reactant concentration $\frac{dx}{dt}$, as shown in Eq. (1).

$$\frac{dT}{dt} = \frac{m_x \Delta H_x}{Mc_p} \cdot \left| \frac{dx}{dt} \right| \tag{1}$$

where $m_x$ is the mass of the reactant of the side reaction, $\Delta H_x$ represents the reaction enthalpy of the side reaction, $M = 1.12$ kg is the mass of the battery, and $c_p = 1100\ \mathrm{J \cdot kg^{-1} \cdot K^{-1}}$ is the specific heat capacity.

The change of the reactant concentration can be calculated by Eq. (2).

$$\frac{dx}{dt} = -kx^n \tag{2}$$

where $k$ is the reaction rate determined by the Arrhenius equation, as shown in Eq. (3), and $n$ is the reaction order of side reactions.

$$k = Ae^{-\frac{E_a}{RT}} \tag{3}$$

where $A$ is the pre-frequency factor, $E_a$ represents the activation energy, and $R$ is the ideal gas constant.

As the exothermic reaction rate changes with time, the heat generation rate (Eq. (1)) is integrated from the reaction start time to the end time, as shown in Eq. (4), where $t_0$ is the reaction start time and $t_1$ is the end time of the side reaction.

$$\int_{t_0}^{t_1} \frac{dT}{dt} dt = \int_{t_0}^{t_1} \frac{m_x \Delta H_x}{Mc_p} \left| \frac{dx}{dt} \right| dt \tag{4}$$

By simplifying Eq. (4) by assuming that the reaction concentration at the endpoint is zero, we can get Eq. (5).

$$T_e - T_0 = \frac{m_x \Delta H_x}{Mc_p} x_0 \tag{5}$$

where $T_0$ is the reaction start temperature, $T_e$ is the side reaction end temperature, and $x_0$ represents the initial reaction concentration.

Suppose the reactant concentration at a certain temperature $T$ is $x$, then the Eq. (5) can be rewritten as Eq. (6).

$$T - T_0 = \frac{m_x \Delta H_x}{Mc_p} (x_0 - x) \tag{6}$$

By dividing Eq. (6) by Eq. (5), here obtains Eqs. (7) and (8) (the differential form of Eq. (7)).

$$x = \frac{T_e - T}{T_e - T_0} x_0 \tag{7}$$

$$\frac{dT}{dt} = \frac{T_e - T_0}{x_0} \frac{dx}{dt} \tag{8}$$

Then, substituting the Eqs. (2), (3) and (7) into Eq. (8) can get Eqs. (9) and (10).

$$\frac{dT}{dt} = Ax_0^{n-1}(T_e - T_0) \left( \frac{T_e - T}{T_e - T_0} \right)^n e^{-\frac{E_a}{RT}} \tag{9}$$

$$\ln \left[ \frac{\frac{dT}{dt}}{(T_e - T_0)^n} \right] = \ln \left[ \frac{Ax_0^{n-1}}{(T_e - T_0)^{n-1}} \right] - \frac{E_a}{RT} \tag{10}$$

To simplify the identification and calculation of reaction kinetic parameters, the reaction order $n$ is set as 1, then Eq. (11) is set.

$$\ln \left[ \frac{\frac{dT}{dt}}{T_e - T_0} \right] = \ln A - \frac{E_a}{RT} \tag{11}$$

Finally, by setting $R^* = \frac{\frac{dT}{dt}}{T_e - T_0}$, the kinetics parameters are identified based on the $\ln(R^*) - 1/T$ relationship. The pre-frequency factor $A$ and activation energy $E_a$ of the exothermic reaction are obtained through the slope of the curve and the intercept of the vertical axis, respectively.

#### 4.1.2 Parameters Identification of the Reaction Kinetics Model

The results of adiabatic TR test on LFP batteries at different SOCs show that severe TR occurred in LFP batteries at 50%, 75%, and 100% SOC, but not in the 25% SOC battery. This section identifies the reaction kinetics parameters of the LFP batteries at 50%, 75%, and 100% SOC based on the TR test results.

Firstly, the temperature rate profiles of the battery during the adiabatic TR test are divided into four parts according to the five-stage TR process in outlined Sect. 3.2. The temperature ranges for each stage are shown in Sect. 3.2. The heat generation of Stage II–IV is calculated using Eq. (12). $T_{0,i}$ and $T_{e,i}$ represent the start and end temperature of each stage, respectively, and $A_i$ and $E_{a,i}$ are the pre-frequency factor and activation energy, which can be determined from the $\ln(R^*)$—$1/T$ relationship curves for each stage.

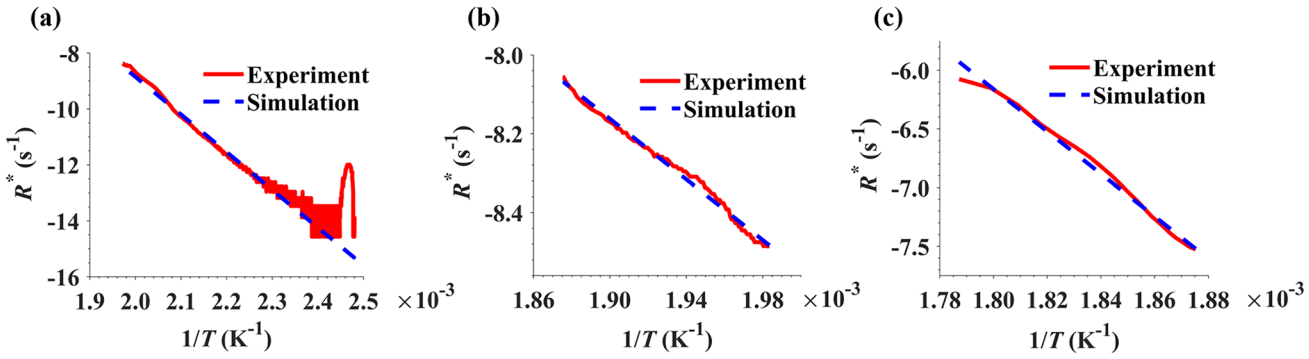


**Fig. 5** The $R^*$ – 1/$T$ profiles of the LFP battery at 100% SOC in each stage. **a** Stage II; **b** Stage III; **c** Stage IV

$$Q_i = \frac{\mathrm{d}T}{\mathrm{d}t} c_p M = A_i (T_{e,i} - T_{0,i}) \left( \frac{T_{e,i} - T}{T_{e,i} - T_{0,i}} \right) \mathrm{e}^{-\frac{E_{a,i}}{RT}} c_p M \left( T_{0,i} < T < T_{e,i} \right) \tag{12}$$

The heat generation in Stage V is typically stems from the extensive internal short circuit and release of electric energy within the battery, which is defined as $Q_{ele}$ in Eq. (13) based on Ref. [42]. The energy released in Stage V, $\Delta H_{ele}$ is determined to be 5.3, 12.6 and 18.8 kJ for batteries at 50%, 75%, and 100% SOC, respectively. The variable $\Delta t$ is used to adjust the maximum temperature rate and is determined to be 900, 50 and 42 s for the battery at 50%, 75%, and 100% SOC, respectively. Finally, the total heat generation during the TR process is calculated by summing the heat generation of each stage, as shown in Eq. (14).

$$Q_{ele}(t) = \frac{1}{\Delta t} (\Delta H_{ele} - \int_0^t Q_{ele}(t) \mathrm{d}t) \tag{13}$$

$$Q_{sum} = Q_{II} + Q_{III} + Q_{IV} + Q_{ele} \tag{14}$$

The reaction kinetics parameters are determined by fitting the $\ln(R^*) - 1/T$. The results for the battery at 100% SOC are presented in Fig. 5 as examples. The simulation results align well with the experimental results, indicating that the reaction kinetics model accurately reflects the heat generation of the battery. Table 3 compares the kinetics parameters of LFP batteries at different SOCs. For the exothermic reaction in Stage II, the activation energies of batteries at different SOCs are all around 110–113 kJ·mol$^{-1}$, indicating a similar exothermic reaction at the start of the self-heating process. In Stage III, the activation energy of the exothermic reaction decreases as the SOC increases, particularly when SOC increases from 50% to 75%. A lower activation energy represents a lower energy barrier required for the reaction, leading to a faster reaction rate. That indicates that the reaction rate in Stage III accelerates as battery SOC increases, consistent with the temperature rate profiles in Fig. 3. A similar trend is observed in Stage IV, where the activation energy for the exothermic reaction in the 100% SOC battery is 143.03 kJ·mol$^{-1}$, significantly lower than that of the 75% SOC battery.

**Table 3** Identified reaction kinetic parameters in TR process of LFP batteries at different SOCs

| SOC (%) | Stage | $A$ (1·s$^{-1}$) | $E_a$ (kJ·mol$^{-1}$) |
|---|---|---|---|
| 50 | II | $6.134\times10^{8}$ | 112.78 |
| | III | $9.50\times10^{6}$ | 103.21 |
| 75 | II | $1.5308\times10^{7}$ | 110.69 |
| | III | $1.4772\times10^{2}$ | 80.937 |
| | IV | $5.4234\times10^{13}$ | 171.05 |
| 100 | II | $1.8066\times10^{8}$ | 111.91 |
| | III | $1.0569\times10^{5}$ | 78.521 |
| | IV | $5.6933\times10^{11}$ | 143.03 |

## 4.2 Model Validation

TR models for the LFP batteries at different SOCs are built using the reaction kinetics parameters identified above. Figure 6 and Table 4 compare the simulated and experimental TR behaviors. As the models only simulate the batteries' heat generation after $T_1$, only the temperature changes after $T_1$ are presented in Fig. 6(a)–(c), and the temperature rate profiles are compared in Fig. 6(d)–(f).

As shown in Fig. 6, the simulated temperature and temperature rate profiles match the experimental results well, although errors increase as the TR process end and the EV-ARC system enters the "Cool" mode. The errors during the cooling stage increase with battery SOC, due to the changes in the tested batteries' specific heat capacities after venting during the ARC tests, which are constant in the model. As this study mainly focuses on the evolutions of battery temperature and temperature rate during the TR process, the model accurately predicts the LFP battery TR behaviors at three different SOCs. Table 4 further

compares the simulated and experimental characteristic temperature of the LFP batteries. The model can also capture the TR characteristic temperatures well, especially for $T_2$ and $T_3$, with the errors less than 3%.

In summary, the proposed modeling approach in this paper presents excellent accuracy in simulating the TR features of LFP batteries at different SOCs, and can be applied in the model-based safety design and optimization of cell, module, and battery systems.

Further validation of the proposed TR prediction model is carried out by applying it to predict the TR behavior under oven test conditions, which is different from the EV-ARC test condition and are commonly used in battery safety regulations. The setup of the oven test is illustrated in Fig. 7(a). The EV-ARC first heats the battery to the target temperature at a constant heating rate and then holds it at the target temperature while waiting for the battery to reach it through thermal convection. As the battery surface reaches the target temperature, the EV-ARC will follow the battery's temperature rise and then switch to a "cooling" mode after 30 min. If the battery undergoes TR within the 30-min waiting period, the EV-ARC system switches to the "cooling" mode immediately. 180 °C oven test is performed on a 100% SOC battery to validate the TR model. As shown in Fig. 7(b) and (c), the model predicted results using the kinetics parameters from Table 3 are consistent with the experimental results. Moreover, the predicted characteristic temperature ($T_2$ and $T_3$) of the battery TR during the 180 °C oven test are 236.1 °C and 683.1 °C, respectively, also consistent with the experimental results ($T_2 = 237.1$ °C, $T_3 = 689.2$ °C), with errors less than 1%.

In summary, the proposed modeling approach in this paper demonstrates excellent accuracy in simulating the TR features of LFP batteries at different SOCs and can

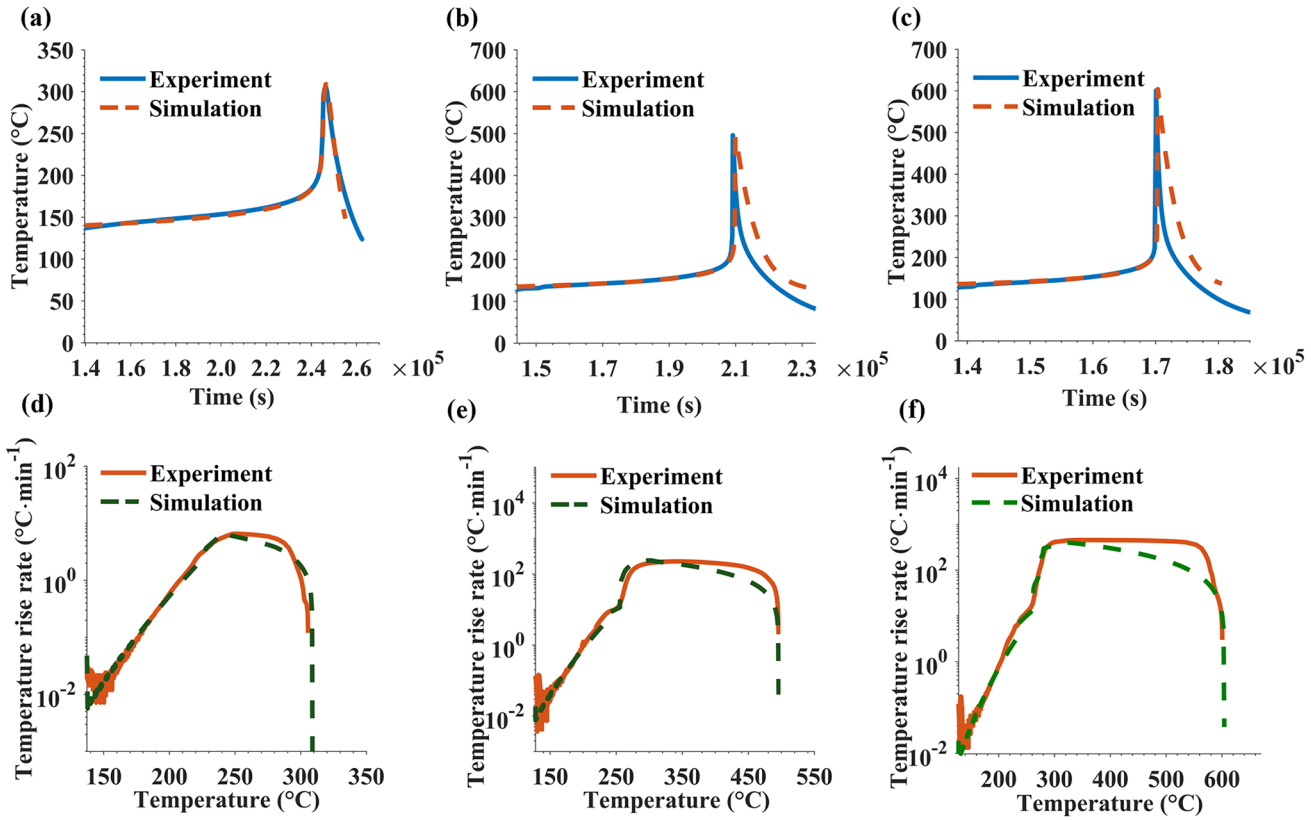


**Fig. 6** Comparison of simulation and experimental TR results of LFP batteries at different SOCs: **a**, **d** 50% SOC; **b**, **e** 75% SOC; **c**, **f** 100% SOC

**Table 4** Comparison of the simulated and experimental TR characteristic temperature in LFP batteries

| SOC (%) | Experimental results | | | Simulation results | | |
|---|---|---|---|---|---|---|
| | $T_1$ (°C) | $T_2$ (°C) | $T_3$ (°C) | $T_1$ (°C) | $T_2$ (°C) | $T_3$ (°C) |
| 50 | 136.1 | 234.6 | 305.8 | 137.2 | 235.4 | 308.7 |
| 75 | 135.9 | 228.6 | 496.2 | 127.9 | 229.8 | 495.8 |
| 100 | 135.9 | 221.4 | 619.9 | 127.9 | 222.9 | 603.9 |

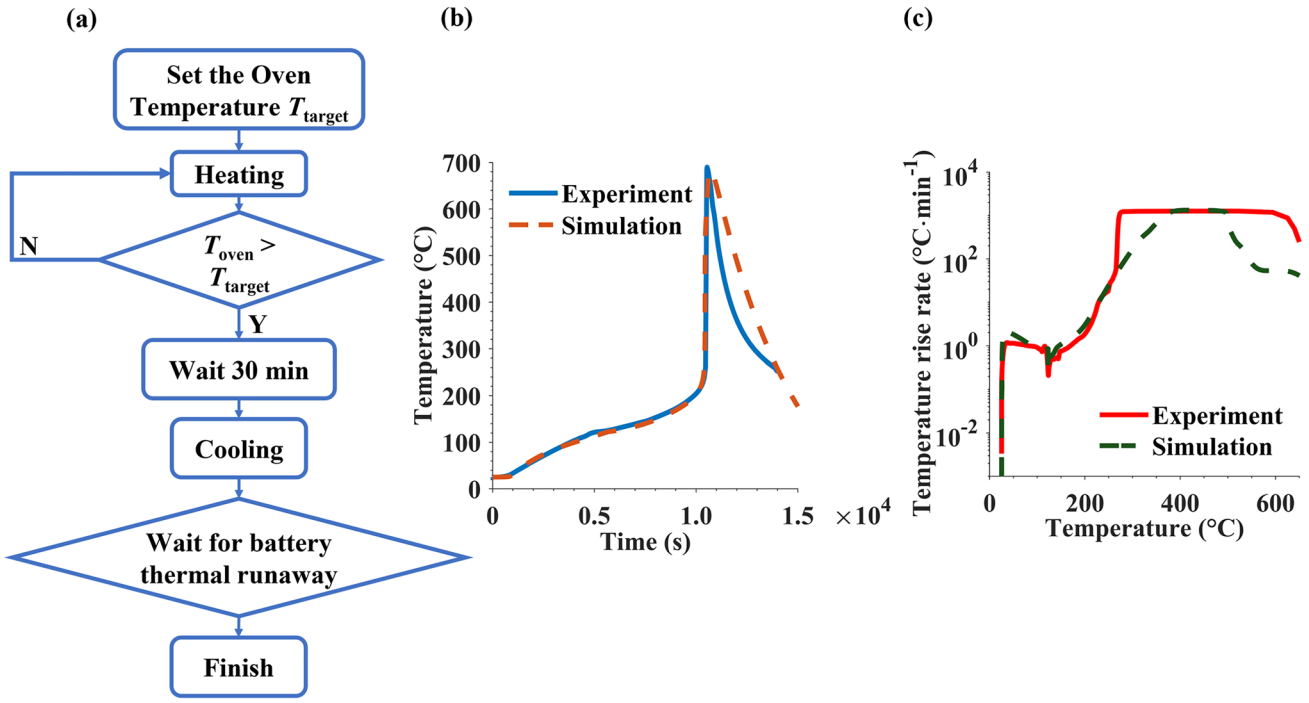


**Fig. 7** Oven experiment process and model verification: **a** Oven test configuration, **b** and **c** Comparison of simulation and experimental TR results for 100% SOC LFP battery under 180 °C oven test conditions

also accurately predict the battery TR behaviors under oven test conditions. This highlights its potential for use in the model-based safety design and optimization of the cell**,** module, and battery systems.

## 5 Conclusions

In this study, the TR behaviors of LFP batteries at different SOCs are investigated based on adiabatic TR test results obtained through the use of an EV-ARC. The results show that $T_1$ decreases from 151.1 to 136 ℃ as the SOC increases, primarily affected by the thermal stability of SEI film. $T_2$ stays constant at around 220–230 ℃ for the batteries under various SOCs. $T_3$ and the maximum temperature rate rise sharply with battery SOC, indicating that the TR severity in the LFP battery increase significantly with increasing SOC. The TR processes in the LFP batteries are divided into five stages according to the evolution of battery temperature rise rate. The reaction kinetics parameters are identified from the TR test results using a $R^*$—plot approach, and TR models are then established to simulate the TR behaviors of the LFP batteries at different SOCs. The models results show excellent accuracy in capturing the TR characteristics in LFP batteries, fitting well with the adiabatic TR test results. The simulated TR characteristic temperatures also agree well with experimental results, especially for $T_2$ and $T_3$, with errors less than 3%. Furthermore, the model demonstrates accurate predictions of battery TR behaviors under oven test conditions, with prediction errors of $T_2$ and $T_3$ less than 1%. Future work will focus on correlating the kinetics parameters with the reaction mechanisms to provide in-depth guidance for safety design and optimization of LFP batteries.

**Acknowledgements** This work was supported by the Key-Area Research and Development Program of Guangdong Province (2020B0909030001), the National Natural Science Foundation of China (52007099, 52076121 and 52177217), and China Postdoctoral Science Foundation (2020M680550). Dongsheng Ren thanks the support from Young Elite Scientists Sponsorship Program by CAST [No. YESS20220063].

## Declarations

**Conflict of interest** On behalf of all the authors, the corresponding author states that there is no conflict of interest.

## References


1. Feng, X., Ren, D., He, X., et al.: Mitigating thermal runaway of lithium-ion batteries. Joule **4**(4), 743–770 (2020)
2. Huang, L., Zhang, Z., Wang, Z., et al.: Thermal runaway behavior during overcharge for large-format lithium-ion batteries with different packaging patterns. J. Energy Storage **25**, 100811 (2019)
3. Lai, X., Chen, Q., Tang, X., et al.: Critical review of life cycle assessment of lithium-ion batteries for electric vehicles: a lifespan perspective. eTransportation **12**, 100169 (2022)
4. Xu, C., Li, L., Xu, Y., et al.: A vehicle-cloud collaborative method for multi-type fault diagnosis of lithium-ion batteries. eTransportation **12**, 100172 (2022)
5. Hao, X., Yuan, Y., Wang, H., et al.: Plug-in hybrid electric vehicle utility factor in China cities: influencing factors, empirical research, and energy and environmental application. eTransportation **10**, 100138 (2021)
6. Hu, X., Yuan, H., Zou, C., et al.: Co-estimation of state of charge and state of health for lithium-ion batteries based on fractional-order calculus. IEEE Trans. Veh. Technol. **67**(11), 10319–10329 (2018)
7. Kong, X., Lu, L., Yuan, Y., et al.: Foreign matter defect battery and sudden spontaneous combustion. eTransportation **12**, 100170 (2022)
8. Hu, G., Huang, P., Bai, Z., et al.: Comprehensively analysis the failure evolution and safety evaluation of automotive lithium ion battery. eTransportation **10**, 100140 (2021)
9. Kovachev, G., Ellersdorfer, C., Gstrein, G., et al.: Safety assessment of electrically cycled cells at high temperatures under mechanical crush loads. eTransportation **6**, 100087 (2020)
10. Duh, Y.S., Theng, J.H., Chen, C.C., et al.: Comparative study on thermal runaway of commercial 14500, 18650 and 26650 $LiFePO_4$ batteries used in electric vehicles. J. Energy Storage **31**, 101580 (2020)
11. Shi, W., Hu, X., Wang, J., et al.: Analysis of thermal aging paths for large-format $LiFePO_4$ /graphite. Electrochim. Acta **196**, 13–23 (2016)
12. Li, L.: $LiFePO_4$ battery becomes a new favorite in the market. China Energy News http.://www.cnenergynews.cn/guonei/2021/11/03/detail_20211103109913.html(2021) Accessed 03 November 2021
13. Meng, X., Yang, K., Zhang, M., et al.: Experimental study on combustion behavior and fire extinguishing of lithium iron phosphate battery. J. Energy Storage **30**, 101532 (2020)
14. Feng, X., Ouyang, M., Liu, X., et al.: Thermal runaway mechanism of lithium ion battery for electric vehicles: a review. Energy Storage Mater. **10**, 246–267 (2017)
15. Wang, Q.S., Ping, P., Zhao, X.J., et al.: Thermal runaway caused fire and explosion of lithium ion battery. J. Power Sources **208**, 210–224 (2012)
16. Ren, D., Feng, X., Han, X., et al.: Recent progress on evolution of safety performance of lithium-ion battery during aging process. Energy Storage Sci. Technol. **7**(6), 957–966 (2018)
17. Sun, L., Wei, C., Guo, D., et al.: Comparative study on thermal runaway characteristics of lithium iron phosphate battery modules under different overcharge conditions. Fire Technol. **56**(4), 1555–1574 (2020)
18. Fernandes, Y., Bry, A., de Persis, S.: Identification and quantification of gases emitted during abuse tests by overcharge of a commercial li-ion battery. J. Power Sources **389**, 106–119 (2018)
19. Huang, Z., Li, H., Mei, W., et al.: Thermal runaway behavior of lithium iron phosphate battery during penetration. Fire Technol. **56**(6), 2405–2426 (2020)
20. Zaghib, K., Dube, J., Dallaire, A., et al.: Enhanced thermal safety and high power performance of carbon-coated $LiFePO_4$ olivine cathode for li-ion batteries. J. Power Sources **219**, 36–44 (2012)
21. Liu, P., Liu, C., Yang, K., et al.: Thermal runaway and fire behaviors of lithium iron phosphate battery induced by overheating. J. Energy Storage **31**, 101714 (2020)
22. Bugryniec, P.J., Davidson, J.N., Brown, S.F.: Assessment of thermal runaway in commercial lithium iron phosphate cells due to overheating in an oven test. Energy Procedia **151**, 74–78 (2018)
23. Hatchard, T.D., MacNeil, D.D., Basu, A., et al.: Thermal model of cylindrical and prismatic lithium-ion cells. J. Electrochem. Soc. **148**(7), A755–A761 (2001)
24. Kim, G.H., Pesaran, A., Spotnitz, R.: Three-dimensional thermal abuse model for lithium-ion cells. J. Power Sources **170**(2), 476–489 (2007)
25. Feng, X., He, X., Ouyang, M., et al.: A coupled electrochemical-thermal failure model for predicting the thermal runaway behavior of lithium-ion batteries. J. Electrochem. Soc. **165**(16), A3748–A3765 (2018)
26. Ren, D., Xiang, L., Feng, X., et al.: Model-based thermal runaway prediction of lithium-ion batteries from kinetics analysis of cell components. Appl. Energy **228**, 633–644 (2018)
27. Liang, G., Zhang, Y., Han, Q., et al.: A novel 3d-layered electrochemical-thermal coupled model strategy for the nail-penetration process simulation. J. Power Sources **342**, 836–845 (2017)
28. Chiu, K.C., Lin, C.H., Yeh, S.F., et al.: An electrochemical modeling of lithium-ion battery nail penetration. J. Power Sources **251**, 254–263 (2014)
29. Zhang, M., Feng, X., Ouyang, M., et al.: Experiments and modeling of nail penetration thermal runaway in a NCM li-ion power battery. Automot. Eng. **37**(7), 743–750756 (2015)
30. Guo, G., Bo, L., Bo, C., et al.: Three-dimensional thermal finite element modeling of lithium-ion battery in thermal abuse application. J. Power Sources **195**(8), 2393–2398 (2010)
31. Peng, P., Jiang, F.: Thermal safety of lithium-ion batteries with various cathode materials: a numerical study. Int. J. Heat Mass Transf. **103**, 1008–1016 (2016)
32. Mei, W., Duan, Q., Wang, Q., et al.: Thermal runaway simulation of large scale lithium iron phosphate battery at elevated temperature. Energy Storage Sci. Technol. **10**(1), 202–209 (2021)
33. Xu, C., Feng, X., Huang, W., et al.: Internal temperature detection of thermal runaway in lithium-ion cells tested by extended-volume accelerating rate calorimetry. J. Energy Storage **31**, 101670 (2020)
34. Feng, X., Fang, M., He, X., et al.: Thermal runaway features of large format prismatic lithium ion battery using extended volume accelerating rate calorimetry. J. Power Sources **255**, 294–301 (2014)
35. Zheng, Y., Shi, Z., Ren, D., et al.: In-depth investigation of the exothermic reactions between lithiated graphite and electrolyte in lithium-ion battery. J. Energy Chem. **69**, 593–600 (2022)
36. Ren, D., Hungjen, H., Li, R., et al.: A comparative investigation of aging effects on thermal runaway behavior of lithium-ion batteries. eTransportation **2**, 100034 (2019)
37. Ren, D., Feng, X., Liu, L., et al.: Investigating the relationship between internal short circuit and thermal runaway of lithium-ion batteries under thermal abuse condition. Energy Storage Mater. **34**, 563–573 (2021)
38. Richard, M.N., Dahn, J.R.: Accelerating rate calorimetry study on the thermal stability of lithium intercalated graphite in electrolyte II. modeling the results and predicting differential scanning calorimeter curves. J. Electrochem. Soc. **146**(6), 2078–2084 (1999)
39. Wang, X., Mohamedi, M.: Accelerating-rate-calorimetry study on the thermal stability of laminated lithium-ion polymer cells. J. Propul. Power **22**(5), 1135–1137 (2006)

40. Feng, X., Sun, J., Ouyang, M., et al.: Characterization of large format lithium ion battery exposed to extremely high temperature. J. Power Sources **272**, 457–467 (2014)
41. Yang, H., Bang, H., Amine, K., et al.: Investigations of the exothermic reactions of natural graphite anode for li-ion batteries during thermal runaway. J. Electrochem. Soc. **152**(1), A73–A79 (2005)
42. Chen, J., Rui, X., Hungjen, H., et al.: Thermal runaway modeling of $LiNi_{0.6}Mn_{0.2}Co_{0.2}O_2$/graphite batteries under different states of charge. J. Energy Storage **49**, 104090 (2022)

**Tao Sun** received his Ph.D. degree in the School of Mechanical Engineering from Shanghai Jiao Tong University in 2006. He is an associate professor at the Department of Automotive Engineering, School of Mechanical Engineering, University of Shanghai for Science and Technology. He has presided over or participated in more than 20 projects, including the Shanghai Natural Science Foundation Project, the key basic research project of the Shanghai Science and Technology Commission, and the key research and innovation project of the Shanghai Education Commission. His research interests include intelligent management of lithium-ion batteries and big data analysis technology.

**Luyan Wang** graduated from the University of Shanghai for Science and Technology with a bachelor's degree in 2020. He is studying for a master's degree in the Department of Automotive Engineering, University of Shanghai for Science and Technology. His research interests include the detection and modeling of lithium plating in lithium-ion batteries.

**Dongsheng Ren** received his Ph. D. degree from the School of Vehicle and Mobility, Tsinghua University, in 2020. He is a postdoctoral researcher at the Institute of Nuclear and New Energy Technology in Tsinghua University, and has received the Young Elite Scientists Sponsorship Program by CAST. His research interests include life cycle thermal runaway characteristics of Li-ion batteries, multi-scale modeling of Li-ion batteries and solid-state Li-ion batteries.

**Yuejiu Zheng** received his Ph.D. degree in Power Engineering and Engineering Thermophysics from Tsinghua University in 2014. He is the deputy director and professor of the Department of Automotive Engineering, School of Mechanical Engineering, University of Shanghai for Science and Technology. He has received the Shanghai "S&T Youth Rising-star Program" and serves as the director of the Whole Life Cycle Joint Research Center of the University of Shanghai for Science and Technology. His research interests include the grouping system of power batteries for new energy vehicles.

**Minggao Ouyang** is a professor at Tsinghua University and an Academician of the Chinese Academy of Sciences. Prof. Ouyang is the leader of the New Energy Powertrain System Group at Tsinghua University, where he has been dedicated to the research of New Energy Power Systems and Transportation Electrification. From 2007 to 2021, Prof. Ouyang has been the chief scientist of the China National Key R&D Program of New Energy Vehicles, and has made significant contributions to the world-leading development of new energy vehicles in China. Prof. Ouyang has made a series of scientific research achievements in Engine Control and Hybrid Powertrains, PEM Fuel Cell Powertrain and Hydrogen Systems, Lithium-ion Battery Safety Design and Management, and Energy Storage and Smart Energy Systems, promoting considerable economic benefits of over 10 billion yuan. He has won more than 10 domestic and foreign science and technology awards, and incubated more than 20 startups (including several companies listed in STAR Market). Prof. Ouyang has published more than 400 SCI papers with a total citation of more than 20,000 times, and has been listed as the Highly Cited Researcher by Clarivate Analytics several times.